AGU PUBLICATIONS

Geophysical Research Letters

RESEARCH LETTER
10.1002/2014GL059299

Key Points:
- Simulation identifies widespread three-dimensional anisotropic turbulence
- Notable turbulence occurs outside of cloud
- Results important for aviation safety and stratosphere-troposphere exchange

Correspondence to:
T. P. Lane,
tplane@unimelb.edu.au

Citation:
Lane, T. P., and R. D. Sharman (2014), Intensity of thunderstorm-generated turbulence revealed by large-eddy simulation, *Geophys. Res. Lett.*, *41*, 2221–2227, doi:10.1002/2014GL059299.

Received 16 JAN 2014
Accepted 27 FEB 2014
Accepted article online 3 MAR 2014
Published online 25 MAR 2014

Intensity of thunderstorm-generated turbulence revealed by large-eddy simulation

Todd P. Lane[1] and Robert D. Sharman[2]

[1]School of Earth Sciences and ARC Centre of Excellence for Climate System Science, University of Melbourne, Melbourne, Victoria, Australia, [2]Research Applications Laboratory, National Center for Atmospheric Research, Boulder, Colorado, USA

Abstract Thunderstorms are characterized by turbulent processes that constitute an important aviation hazard and cause vertical transport of atmospheric constituents. Turbulence occurs within cloud and in the surrounding clear air, but, despite its importance, the characteristics of thunderstorm-generated turbulence and its spatial distribution are poorly understood, especially outside of cloud. Here we use large-eddy simulation to characterize turbulence generated by a canonical thunderstorm. The simulation identifies regions of notable three-dimensional anisotropic turbulence more than 5 km above the storm, in a shallow layer above the storm's anvil, and a horizontally asymmetric pattern of weaker turbulence that extends more than 50 km horizontally away from the cloud. Our results provide the first continuous estimate of turbulence intensity in and around thunderstorms and represent a major step toward improved turbulence avoidance methods. The results have broader implications for understanding the fundamental aspects of how thunderstorms affect their environment through vertical exchange processes.

1. Introduction

Thunderstorm-generated turbulence is an important aviation hazard and is a major cause of occupant injuries, occasional aircraft damage, and additional operational costs to the airlines [*Kaplan et al.*, 2005; *Lane et al.*, 2012; *Sharman et al.*, 2012]. In-cloud turbulence can be avoided using remote sensing techniques or by simply evading visible cloud. However, thunderstorm-generated turbulence also occurs in the clear air outside of cloud (so-called near-cloud turbulence, NCT); NCT is difficult to identify using standard operational technologies and hence is responsible for many unexpected aircraft turbulence encounters. Although turbulence avoidance guidelines exist [*Federal Aviation Administration*, 2012], many studies have shown these to be inadequate and unphysical [*Lane et al.*, 2012; *Trier and Sharman*, 2009; *Trier et al.*, 2012; *Fovell et al.*, 2007], and improved knowledge of turbulence characteristics inside and outside of thunderstorms is required to properly quantify the risks.

Thunderstorm-generated turbulence is also of fundamental importance because it contributes to mixing and stratosphere-troposphere exchange (STE) [*Holton et al.*, 1995; *Hegglin et al.*, 2004; *Tang et al.*, 2011; *Homeyer et al.*, 2014], a process that helps determine the radiative budget of the global climate. It is well established that thunderstorms transport lower-tropospheric air vertically and deposit near-surface chemical species, including water, into the stratosphere [*Mullendore et al.*, 2005; *Wang*, 2003]. Observations also identify downward transport of stratospheric air near thunderstorms [*Poulida et al.*, 1996], which is a major source of tropospheric ozone [*Tang et al.*, 2011]. Turbulence around thunderstorms is likely to play a key role in the downward exchange process because observations suggest that the transport of ozone occurs at the margins of thunderstorm anvils [*Poulida et al.*, 1996], but the processes governing this exchange remain mostly unresolved.

Studies using numerical simulations to understand NCT have shown its generation to be related to gravity wave instabilities [*Lane et al.*, 2012; *Fovell et al.*, 2007] and dynamical (Kelvin-Helmholtz) instabilities [*Trier and Sharman*, 2009; *Zovko-Rajak and Lane*, 2014]. Even though those efforts have simulated turbulence occurrence, the models were unable to properly estimate turbulence intensity because of their coarse resolution or use of only two dimensions. Although observations are essential, they are generally absent within the convective region of storms and normally too sparse elsewhere. Accordingly, there are no continuous estimates of the relative intensity of turbulence in different parts of storms or the clear air surrounding them. Numerical simulation offers the best opportunity to obtain these continuous intensity estimates [*Lane et al.*, 2012; *Sharman et al.*, 2012].

Simulating NCT is challenging because it requires modeling of microphysical processes as well as many decades of scale, viz. the organized storm circulation (~10–~500 km) [*Weisman et al*., 1997], the convective updrafts (~1–~10 km) [*Bryan et al*., 2003], and the scales of motion that affect large aircraft (~100 m–~2 km) [*Lane et al*., 2012]. For example, *Bryan et al*. [2003] showed that ~100 m grid spacing is required to begin to resolve the turbulent eddies in deep convective systems. Here we use large-eddy simulation (LES) (wherein the larger higher energy-containing turbulent eddies are explicitly resolved but the smaller less energetic eddies are parameterized) to examine the spatial distribution of turbulence intensity for an idealized three-dimensional thunderstorm. The simulation is extremely computationally intensive and with 75 m grid spacing is able to begin to resolve scales of motion that affect large aircraft. We present the results from one simulation of a canonical squall line and present data at the end of a 6 h simulation when the system is mature. The simulation domain is very large, and the horizontal grid spacing of 75 m is about an order of magnitude finer than most previous three-dimensional simulations of deep convection and convectively induced turbulence. This configuration allows us to capture the larger scales relevant for the convection processes and resolve the turbulence in three dimensions. Using these results, we are able to quantify, for the first time, the spatial distribution of turbulence intensity inside and outside of thunderstorms.

2. Methods

We use the CM1 (Cloud Model 1) finite difference model [*Bryan et al*., 2003] in a configuration that builds upon previous studies [*Bryan et al*., 2003; *Weisman et al*., 1997]. The domain is 600 km long in the across-line (x) direction, 90 km wide in the along-line (y) direction, and 25 km deep in the vertical (z); the grid spacing (Δ) is 75 m (i.e., the domain size is $8000 \times 1200 \times 334$ points). The domain is periodic in y, and the boundaries at $x = 0$ and $x = 600$ km are radiative; damping is applied in the uppermost 9 km to mitigate gravity wave reflections. The large domain size in the x-direction relative to the region of interest and the application of wave emitting boundary conditions minimizes wave reflection from the lateral boundaries, which was verified by visual inspection. The environment is defined by an analytic sounding [*Weisman and Klemp*, 1982] and an across-line wind profile that contains a linear wind change of 10 m s^{-1} in the lowest 2.5 km and unsheared flow aloft. The tropopause is at $z = 12$ km. Convection is initiated using a line thermal parallel to the y axis with imposed random perturbations in the same way as *Bryan et al*. [2003]. Microphysics is parameterized using a bulk scheme with six classes [*Lin et al*., 1983], and sub-grid turbulence is parameterized using a 1.5-order closure [*Deardorff*, 1980]. Although not presented here, in most locations of the simulated storm, the resolved turbulence kinetic energy (constructed from resolved motion with horizontal scales less than 2 km) is at least an order of magnitude larger than the parameterized turbulence kinetic energy, consistent with LES assumptions.

To characterize the turbulence, we calculate the one-dimensional power spectral density in the y-direction for each velocity component (after subtracting the domain average) at each point in the x-z space. One half the sum of the squares of these three components defines the kinetic energy density as a function of wave number k. We also define the isotropy, $I = |\hat{w}|/|\hat{u}|$, where $\hat{w}$ and $\hat{u}$ are the spectral amplitudes of the vertical velocity and x-velocity (i.e., the two transverse components), respectively.

Many commercial aircraft report turbulence intensity by estimating the cube root of the energy dissipation rate, $\varepsilon^{1/3}$, using onboard accelerometer or vertical velocity measurements [*Cornman et al*., 1995; *Sharman et al*., 2013]. Here we estimate it using the relation for the transverse component [*Wyngaard*, 2010], $|\hat{u}|^2(k) = 4/3C\varepsilon^{2/3}k^{-5/3}$, where $|\hat{u}|^2$ is the one-sided spectral density of the x-component of the perturbation wind and $C = 0.5$ [*Sreenivasan*, 1995]. This relation assumes isotropic and homogeneous turbulence, yet it will be shown that the turbulence is anisotropic and in some regions the spectral slopes depart from $k^{-5/3}$; nonetheless, we derive $\varepsilon^{1/3}$ in this way since it is the aviation sector's convention. The International Civil Aviation Authority (ICAO) suggest peak $\varepsilon^{1/3}$ thresholds (when calculated from the vertical acceleration or velocity over 1 min intervals) for the subjective aircraft turbulence intensity categories of "light," "moderate," and "severe" of 0.1, 0.4, and 0.7 $m^{2/3}$ s^{-1} [*International Civil Aviation Organization* [*ICAO*], 2007], but recent comparisons to pilot reports [*Sharman et al*., 2014] suggest that these values may be too large and threshold values of ~0.05 $m^{2/3}$ s^{-1} (light), 0.2 $m^{2/3}$ s^{-1} (moderate), and 0.3–0.5 $m^{2/3}$ s^{-1} (severe) give better agreement to the reports for medium-sized aircraft (though there is some overlap between the categories). Suggested thresholds for $\varepsilon^{1/3}$ calculated from the horizontal velocity are similar [*Dutton*, 1971].

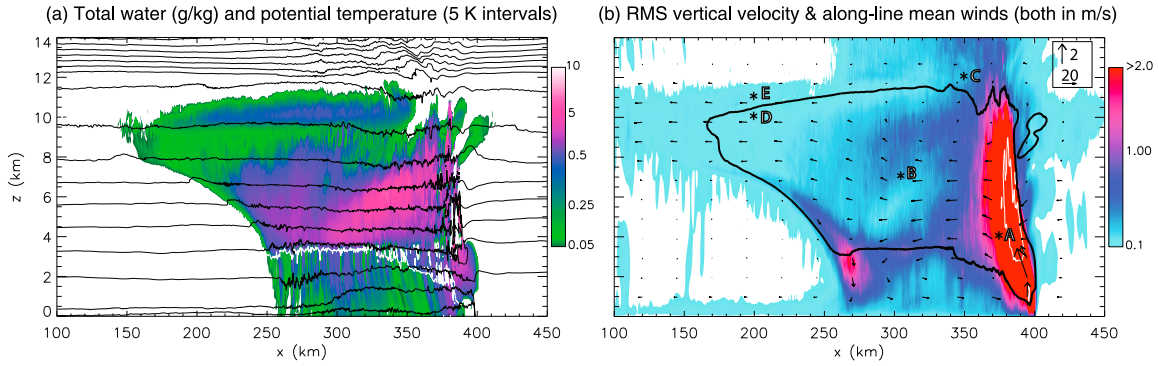

Figure 1. Structure of simulated storm. (a) Across-line cross section (through middle of domain, $y = 45$ km): Total water (liquid plus ice) in colors and potential temperature (defined as $T[1000/p]^{0.286}$, where T is temperature in K and p is pressure in hPa) contours. The white line separates cloud from rain. (b) Along-line mean properties: root mean square (RMS) vertical velocity in colors (the thin white contour is 5 m s^{-1}), cloud outline (black, defined as the 0.1 g kg^{-1} cloud concentration isopleth), and wind vectors. Locations A–E marked in Figure 1b are discussed in text.

We use a similar method to that used for aircraft [*Cornman et al.*, 1995; *Sharman et al.*, 2014] to estimate the turbulence intensity in terms of the peak value of $\varepsilon^{1/3}$. At each point in x-z, we separate the 90 km long series (aligned in the y-direction) into nineteen 9 km long overlapping segments that are each detrended and tapered. For each segment, we calculate the power spectral density of the x-component of the perturbation wind. We then fit a straight line to the spectrum (in log-log space) between horizontal wavelengths of 600 and 2250 m, assuming that the slope of the line follows $k^{-5/3}$. $\varepsilon^{1/3}$ is calculated from the fitted line for each segment, and the peak value is the largest of these at each x-z point. (We use the x-component because it mostly dominates the z-component; the range of scales approximately matches those resolved scales of three-dimensional turbulence [see later] as well as the resolved scales that affect large aircraft).

3. Results

The simulated storm (Figure 1) possesses all of the features of observed storms of this type (viz. leading line, trailing stratiform mesoscale convective systems) [*Houze*, 2004; *Parker and Johnson*, 2004]. The main convective region (near $x = 380$ km) contains maximum water content and mean and RMS vertical velocity. A well-defined anvil exists ($z \gtrsim 8$ km), extending rearward from the convective region (until $x \approx 170$ km). At the rear of the storm below the anvil is a region of descent, viz. the mesoscale downdraft, that culminates in a localized maximum in RMS vertical velocity (near $x,z = 270, 2$ km). The system develops an organized across-line flow, dominated by front to rear ascending air that forms an upper-level rearward moving outflow jet with maximum vertical shear at the vertical margins of the anvil.

The RMS vertical velocity identifies regions of instability, waves, and turbulence (Figure 1b) that extend well beyond the cloudy air, especially evident in the upper-level outflow at the front and rear of the storm, below the anvil, and in the stratosphere above the convective region. The potential temperature (Figure 1a) identifies large-amplitude gravity waves [e.g., *Lane et al.*, 2012; *Trier et al.*, 2012] above the convective region and immediately ahead of the storm, e.g., $(x,z) = (360,12)$ km and $(x,z) = (390,8)$ km, respectively. Small-scale structures in the potential temperature contours (in Figure 1a) are indicative of turbulence.

The spatial patterns of vertical velocity and vorticity in the upper troposphere (Figure 2) expose the complex formations that exist within and outside of cloud. Coherent vertical velocity structures occur throughout the anvil with a variety of orientations, with the intense small-scale perturbations highlighted by collocated maxima in vorticity. The vorticity maxima have contributions from all three directional components (not shown) and extend more than 50 km outside of the cloud boundary both ahead and behind the storm. Of relevance is that many of the vorticity maxima outside the anvil appear stronger and more widespread than those within it. At the margins of influence of the storm, where the vorticity becomes small, the velocity becomes dominated by gravity waves that appear as interfering curved wavefronts.

At the smaller scales resolved by the simulation, the kinetic energy spectrum is expected to follow a power law relationship over the inertial range such that $E(k) \sim k^{-5/3}$, where k is the horizontal wave number,

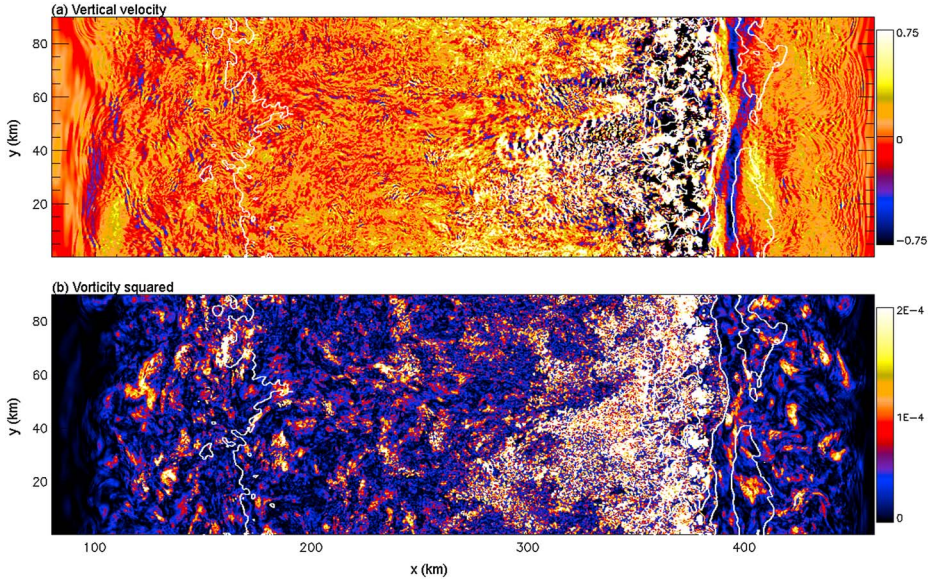

Figure 2. Horizontal patterns of turbulence in the upper-troposphere inside and outside of cloud. (a) Vertical velocity (in m s^{-1}) and (b) the square of the vorticity magnitude (in s^{-2}) at a constant altitude of 10 km. The cloud outline, defined as the 0.1 g kg^{-1} isopleth of cloud concentration, is shown with white lines; cloud encompasses most of the region from $180 < x < 380$ km, and the main convective region is approximately $350 < x < 380$ km.

assuming homogeneous isotropic turbulence [*Kolmogorov*, 1941; *Wyngaard*, 2010]. Kinetic energy spectra from the simulation (Figure 3) reveal distinct characteristics and amplitudes in different parts of the storm. Spectra for locations in the middle of the storm (B), above the convective region (C), and within the anvil (D) all approximately follow $k^{-5/3}$ at scales shorter than about 6 km. The spectrum within the (unstable) convective region (A) has peaks near 2 km horizontal scale, follows $k^{-5/3}$ at higher wave numbers, and has a shallower slope at lower wave numbers. This spectrum identifies the input of energy at the ~2 km characteristic scale of the convective updrafts. Immediately above the anvil (E), the amplitude is larger at scales less than ~3 km than within it (D), despite the spectra following each other closely at longer scales. At the shorter scales, the spectrum above the anvil (E) is shallower than $k^{-5/3}$, indicating a small-scale input of energy likely due to shear instabilities in this region [e.g., *Zovko-Rajak and Lane*, 2014].

We further examine the characteristics of the turbulence by calculating its isotropy *I* (Figure 3b). For purely isotropic turbulence the ratio of the transverse components has $I = 1$. The main convective region (A) is dominated by vertical motions at the updraft scales, with maximum *I* at approximately 2.5 km. At scales between 600 m and 1 km the motions in the convective region are very close to isotropic, and below those scales the motions become poorly resolved. The turbulence above the convective region (C) is nearly

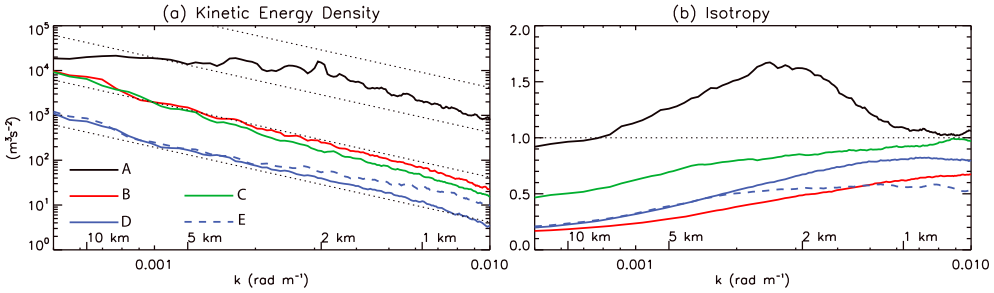

Figure 3. Spectral properties of velocity perturbations in different parts of the storm. (a) Kinetic energy density and (b) the corresponding isotropy, *I*, versus along-line horizontal wave number *k* (truncated at spatial scales of 600 m = 8 × Δ)—the horizontal wavelength is also shown. Each spectrum is averaged horizontally over 50 km in the across-line direction, centered on the locations A–E in Figure 1b; dotted lines in Figure 3a follow $k^{-5/3}$.

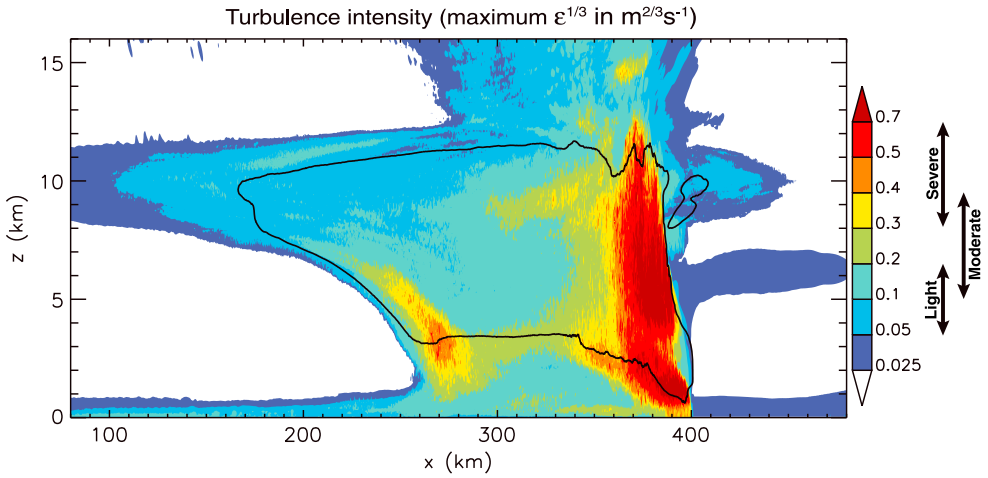

Figure 4. Spatial distribution of along-line maximum turbulence. Peak $\varepsilon^{1/3}$ determined from data obtained during the last 30 min of the simulation (colors). Also shown is the along-line mean cloud outline (defined as in Figure 1b). Approximate turbulence categories based on recent comparisons to pilot reports [*Sharman et al.*, 2014] are also shown.

isotropic at the minimum resolvable scale, indicating convective instability associated with gravity wave breaking and implying efficient vertical mixing in this region [e.g., *Wang*, 2003]. Horizontal motion dominates all other locations of the storm since outside the convective regions the flow has finite (albeit small) mean static stability, which has the effect of inhibiting vertical motion. Nonetheless, for these locations at scales less than about 3 km, l approaches unity. A similar transition has been identified in aircraft observations [*Schumann et al.*, 1995]. Although not shown, wave number spectra of only the vertical velocity show a resolved inertial range at these short scales, i.e., we are resolving the largest eddies. Nonetheless, even though our calculation is enormously computationally intensive we are still only resolving less than a decade in horizontal scale of three-dimensional turbulence.

In Figure 4, we show the calculated spatial distribution of along-line-maximum turbulence intensity (peak $\varepsilon^{1/3}$). As expected, the strongest turbulence occurs within the convective region over the entire depth of the storm, with the absolute peak corresponding to the main updraft region (Figure 1). We also identify notable turbulence just inside of cloud under the anvil within the strongly sheared mesoscale downdraft region. Broad regions of turbulence are present in the upper-level outflow regions, with more extensive turbulence to the rear, and above the storm in the wave-dominated region. Local intensity maxima occur above the storm in the wave region due to wave steepening and local convective instabilities (viz. breaking) [*Lane et al.*, 2012; *Trier et al.*, 2012] and immediately above the anvil related to shear instabilities caused by the storm-induced flow [*Trier and Sharman*, 2009; *Zovko-Rajak and Lane*, 2014]. At least some of the turbulence in the upper outflow is likely formed within the cloud and advected horizontally, but turbulence above the anvil and in the wave region above the storm probably form due to local instabilities in those locations. All of these turbulent regions coincide with the cruise altitudes of commercial aircraft and are also of fundamental importance for STE [*Holton et al.*, 1995] because they are near the tropopause where the vertical gradients in constituent species are large. The intensities are consistent with research aircraft observations [*Meischner et al.*, 2001], and moderate or stronger turbulence has been encountered by commercial aircraft in these out-of-cloud locations [*Kim and Chun*, 2012; *Trier and Sharman*, 2009; *Lane et al.*, 2012]. Notably, the spatial extent of turbulence and its intensity relative to other parts of the storm has never been properly determined before now.

4. Conclusions

Our results identify locations outside of cloud that are more turbulent than some locations within it. We identify a laterally asymmetric distribution of three-dimensional anisotropic turbulence that extends more than 50 km from the cloud boundary and at least 5 km above the storm, well beyond aviation industry guidelines [*FAA*, 2012]. For this storm, the strongest upper-level out-of-cloud turbulence occurs above the convective part of the storm, followed by a shallow region above the margins of the anvil. These out-of-cloud locations are important for stratosphere-troposphere exchange, and turbulence there would contribute to

the irreversible mixing required to explain the observed stratosphere to troposphere exchange of ozone [*Poulida et al*., 1996]. Future work that incorporates tracers within these simulations is planned to properly quantify the mixing and exchange processes.

Here we have presented only one realization of turbulence generated by a thunderstorm in idealized conditions. Many more simulations of this kind are necessary to explore the sensitivities to mesoscale storm structure and background quantities like wind shear and stability, which will delineate parameters controlling patterns of turbulence and mixing potential. The parameter space is large, and numerous idealized and real simulations are necessary. Nonetheless, our results are a major advance toward properly characterizing the turbulence near thunderstorms and are an important step toward developing new physically based thunderstorm-generated turbulence avoidance guidelines for the aviation industry. Improved guidelines should reduce the risk of unanticipated encounters, which could be incorporated within future automated air traffic management systems. Improved guidelines would also help adapt to any increases in storminess along flight routes associated with climate change, which has already been suggested for CAT [*Williams and Joshi*, 2013].

Acknowledgments

TPL is supported by the Australian Research Council's Future Fellowships (FT0990892) and Centre of Excellence (CE110001028) Schemes. The National Center for Atmospheric Research is sponsored by the National Science Foundation. Computing was conducted on the National Computational Infrastructure (NCI) facility in Canberra through access provided by the merit allocation and flagship schemes. We thank George Bryan (NCAR) for providing the CM1 code (available from: http://www.mmm.ucar.edu/people/bryan/cm1/) and useful discussions. We also thank Ulrich Schumann (DLR), Stan Trier (NCAR), and Dragana Zovko-Rajak (University of Melbourne) for useful discussions and two anonymous reviewers for their comments.

The Editor thanks two anonymous reviewers for assistance in evaluating this manuscript.

References

Bryan, G. H., J. C. Wyngaard, and J. M. Fritsch (2003), Resolution requirements for the simulation of deep moist convection, *Mon. Weather Rev.*, *131*, 2394–2416.

Cornman, L. B., C. S. Morse, and G. Cunning (1995), Real-time estimation of atmospheric turbulence severity from in-situ aircraft measurements, *J. Aircraft*, *32*, 171–177.

Deardorff, J. W. (1980), Stratocumulus-capped mixed layer derived from a three-dimensional model, *Boundary Layer Meteorol.*, *18*, 495–527.

Dutton, J. (1971), Clear-air turbulence, aviation, and atmospheric science, *Rev. Geophys. Space Phys.*, *9*, 613–657.

Federal Aviation Administration (2012), *Aeronautical Information Manual*, Section 7-1-29. [Available at http://www.faa.gov/air_traffic/publications/ATpubs/AIM/index.htm.]

Fovell, R. G., R. D. Sharman, and S. B. Trier (2007), A case study of convectively-induced clear-air turbulence, in *Proc. 12th Conference on Mesoscale Processes*, Amer. Meteor. Soc., Waterville Valley, N. H., 6–9 Aug, Paper 13.4.

Hegglin, M. I., et al. (2004), Tracing troposphere-to-stratosphere transport above a mid-latitude deep convective system, *Atmos. Chem. Phys.*, *4*, 741–756, doi:10.5194/acp-4-741-2004.

Holton, J. R., P. H. Haynes, M. E. McIntyre, A. R. Douglass, R. B. Rood, and L. Pfister (1995), Stratosphere-troposphere exchange, *Rev. Geophys.*, *33*, 403–439.

Homeyer, C. R., L. L. Pan, and M. C. Barth (2014), Transport from convective overshooting of the extratropical tropopause and the role of large-scale lower stratospheric stability, *J. Geophys. Res. Atmos.*, doi:10.1002/2013JD020931, in press.

Houze, R. A., Jr. (2004), Mesoscale convective systems, *Rev. Geophys.*, *42*, RG4003, doi:10.1029/2004RG000150.

International Civil Aviation Organization (ICAO) (2007), Meteorological service for international air navigation, in *Annex 3 to the Convention on International Civil Aviation*, 16th ed., ICAO (International Civil Aviation Organization), 187 pp. [Available at http://www.wmo.int/pages/prog/www/ISS/Meetings/CT-MTCDF-ET-DRC_Geneva2008/Annex3_16ed.pdf.]

Kaplan, M. L., A. W. Huffman, K. M. Lux, J. J. Charney, A. J. Riordan, and Y.-L. Lin (2005), Characterizing the severe turbulence environments associated with commercial aviation accidents. Part 1: A 44-case study synoptic observational analyses, *Meteorol. Atmos. Phys.*, *88*, 129–152.

Kim, J.-H., and H.-Y. Chun (2012), A numerical simulation of convectively induced turbulence above deep convection, *J. Appl. Meteorol. Climatol.*, *51*, 1180–1200.

Kolmogorov, A. N. (1941), The local structure of turbulence in an incompressible fluid at very high Reynolds numbers, *Dokl. Akad. Nauk. SSSR*, *30*, 301–305.

Lane, T. P., R. D. Sharman, S. B. Trier, R. G. Fovell, and J. K. Williams (2012), Recent advances in the understanding of near-cloud turbulence, *Bull. Am. Meteorol. Soc.*, *93*, 499–515.

Lin, Y.-L., R. D. Farley, and H. D. Orville (1983), Bulk parameterization of the snow field in a cloud model, *J. Climate Appl. Meteorol.*, *22*, 1065–1092.

Meischner, P., R. Baumann, H. Höller, and T. Jank (2001), Eddy dissipation rates in thunderstorms estimated by Doppler radar in relation to aircraft in situ measurements, *J. Atmos. Oceanic Technol.*, *18*, 1609–1627.

Mullendore, G. L., D. R. Durran, and J. R. Holton (2005), Cross-tropopause tracer transport in midlatitude convection, *J. Geophys. Res.*, *110*, D06113, doi:10.1029/2004JD005059.

Parker, M. D., and R. H. Johnson (2004), Structures and dynamics of quasi-2D mesoscale convective systems, *J. Atmos. Sci.*, *61*, 545–567.

Poulida, O., R. R. Dickerson, and A. Heymsfield (1996), Stratosphere-troposphere exchange in a midlatitude mesoscale convective complex: 1. Observations, *J. Geophys. Res.*, *101*(3), 6823–6836.

Schumann, U., P. Konopka, R. Baumann, R. Busen, T. Gerz, H. Schlager, P. Schulte, and H. Volkert (1995), Estimate of diffusion parameters of aircraft exhaust plumes near the tropopause from nitric oxide and turbulence measurements, *J. Geophys. Res.*, *100*, 14,147–14,162.

Sharman, R. D., S. B. Trier, T. P. Lane, and J. D. Doyle (2012), Sources and dynamics of turbulence in the upper troposphere and lower stratosphere: A review, *Geophys. Res. Lett.*, *39*, L12803, doi:10.1029/2012GL051996.

Sharman, R. D., L. B. Cornman, G. Meymaris, J. Pearson, and T. Farrar (2014), Description and derived climatologies of automated in situ eddy dissipation rate reports of atmospheric turbulence. *J. Appl. Meteorol. Climatol.*, doi:10.1175/JAMC-D-13-0329.1, in press.

Sreenivasan, K. R. (1995), On the universality of the Kolmogorov constant, *Phys. Fluids*, *7*, 2778–2784.

Tang, Q., M. J. Prather, and J. Hsu (2011), Stratosphere−troposphere exchange ozone flux related to deep convection, *Geophys. Res. Lett.*, *38*, L03806, doi:10.1029/2010GL046039.

Trier, S. B., and R. D. Sharman (2009), Convection-permitting simulations of the environment supporting widespread turbulence within the upper-level outflow of a mesoscale convective system, *Mon. Weather Rev.*, *137*, 1972–1990.

Trier, S. B., R. D. Sharman, and T. P. Lane (2012), Influences of moist convection on a cold-season outbreak of clear-air turbulence (CAT), *Mon. Weather Rev.*, *140*, 2477–2496.

Wang, P. K. (2003), Moisture plumes above thunderstorm anvils and their contributions to cross-tropopause transport of water vapor in midlatitudes, *J. Geophys. Res.*, *108*(D6), 4194, doi:10.1029/2002JD002581.

Weisman, M. L., and J. B. Klemp (1982), The dependence of numerically simulated convective storms on vertical wind shear and buoyancy, *Mon. Weather Rev.*, *110*, 504–520.

Weisman, M. L., W. C. Skamarock, and J. B. Klemp (1997), The resolution dependence of explicitly modeled convective systems, *Mon. Weather Rev.*, *125*, 527–548.

Williams, P. D., and M. M. Joshi (2013), Intensification of winter transatlantic aviation turbulence in response to climate change, *Nat. Clim. Change*, *3*, 644–648.

Wyngaard, J. C. (2010), *Turbulence in the Atmosphere*, pp. 393, Cambridge Univ. Press, Cambridge, U. K., and New York.

Zovko-Rajak, D., and T. P. Lane (2014), The generation of near-cloud turbulence in idealized simulations, *J. Atmos. Sci.*, doi:10.1175/JAS-D-13-0346.1, in press.